Desalination and Water Treatment
www.deswater.com

doi: 10.5004/dwt.2022.28883

273 (2022) 92–103
October

In-situ monitoring of calcium carbonate scale progression on reverse osmosis membranes using Raman spectroscopy

Danielle J. Park[a], Omkar D. Supekar[a,c], Alan R. Greenberg[a,b], Juliet T. Gopinath[c,d,e,*], Victor M. Bright[a]

[a]*Department of Mechanical Engineering, University of Colorado, Boulder, CO, 80309, USA, emails: danielle.j.park@colorado.edu (D.J. Park), omkar.supekar@colorado.edu (O.D. Supekar), alan.greenberg@colorado.edu (A.R. Greenberg), victor.bright@colorado.edu (V.M. Bright)*
[b]*Membrane Science, Engineering and Technology Center, University of Colorado, Boulder, CO, 80309, USA*
[c]*Department of Electrical, Computer, and Energy Engineering, University of Colorado, Boulder, CO, 80309, USA*
[d]*Department of Physics, University of Colorado, Boulder, CO 80309, USA, email: julietg@colorado.edu (J.T. Gopinath)*
[e]*Materials Science and Energy Engineering, University of Colorado, Boulder, CO 80309, USA*

Received 12 May 2022; Accepted 12 August 2022

ABSTRACT

Direct monitoring techniques of fouling in membrane-based filtration processes can be implemented as part of an effort to reduce the negative effects of membrane fouling. In particular, monitoring techniques with chemical characterization capability are crucial for the formulation of effective fouling prevention and mitigation strategies. In the present work, Raman spectroscopy was applied as an in-situ monitoring technique for calcium carbonate scaling on commercial reverse osmosis membranes. The bench-scale Raman monitoring system allowed for a qualitative chemical assay of the scaled membrane surface at sequential downstream and upstream axial positions. The time evolution of the downstream and upstream calcium carbonate Raman signal was evaluated with respect to computed values of local concentration at the membrane surface, revealing a statistically significant dependence ($p < 0.001$). The real-time Raman data were bolstered by results of post-mortem analysis (scanning electron microscopy, gravimetric measurements, and laser interferometry). The employed technique was capable of detecting crystals with characteristic lengths <50 μm. Preliminary evidence of polymorph detection was also presented with recommendations for improvements in the technique.

Keywords: Calcium carbonate scale progression; Raman spectroscopy; In-situ monitoring; Spatial dependence; Reverse osmosis desalination membrane

1. Introduction

Reverse osmosis (RO) membranes are well suited for the filtration of feed waters containing dissolved salt ions due to an active polyamide layer that is highly crosslinked [1,2]. As a result, an inherent challenge is the crystallization of sparingly soluble salts on the feed side of the membrane [3,4]. In RO desalination of seawater and brackish water, examples of problematic salts can include calcium sulfate, barium sulfate, or calcium carbonate [5]. The deposition and growth of inorganic salts on the surface of RO membranes is a subset of fouling more specifically known as scaling, leading to an increase in operating costs, energy consumption, and the use of additional chemicals formulated to clean, reduce, or delay its occurrence [6]. Scaling also limits the production and quality of the product water.

In an effort to better understand fouling mechanisms and optimize the RO process, a portion of membrane

* Corresponding author.

research is dedicated to development of techniques for direct monitoring [7–15] of membrane fouling. These techniques have been used to detect scaling in its early stages, when remedial actions are most effective [14,16–18], and provide insight into the mechanisms of fouling. For example, visual observation (VO) techniques [14,19–22] have been used to study the kinetics of local gypsum crystal growth and macroscopic crystal coverage, clearly illustrating the spatial nonuniformity of membrane scale coverage. VO is generally limited by a minimum detectable crystal diameter of ~50–100 μm; consequently, incipient scaling crystals are rendered undetectable as they are much smaller [5,23]. Ultrasonic time-domain reflectometry (UTDR) has been employed in inorganic and organic fouling studies, demonstrating sensitivity to changes in the fouling layer [12,24,25]. Although UTDR can provide earlier, more localized information regarding the fouling layer as compared to permeate flux changes, it is difficult to relate sensor signals to specific contributions of distinct components in the fouling layer. Similarly, electrical impedance spectroscopy (EIS) has shown potential as an early-warning tool that can distinguish between the onset and development of both organic and inorganic fouling. Since EIS is an area-averaged measurement, it is challenging to determine to what extent specific foulants in a multicomponent feed are included in the EIS signal [8,26,27]. Area-averaged or global measurements such as EIS and permeate flux can be problematic for monitoring membrane scaling due to the lack of spatial information [7,17,28–30].

Raman spectroscopy [31] is an optical technique based on the inelastic photon-phonon interactions of the incident light source and materials with Raman-active cross-sections. The molecular composition and arrangement of the material dictates the wavelength of the Raman-shifted photons, allowing for chemical identification of the material. Additionally, the spatial resolution of the Raman data, which is related to the diffraction-limited spot size of the employed laser beam [32], facilitates a local measurement which is necessary in the study of spatially nonuniform fouling mechanisms. The use of Raman spectroscopy to detect membrane fouling non-destructively is a recent application, and the technique has been used to demonstrate chemical detection of a variety of foulants, including biofouling [9], organic fouling [10,33], and inorganic fouling [34–36] on RO and UF membranes.

Therefore, the present work implements Raman spectroscopy for membrane scaling detection to address a critical limitation of available direct monitoring techniques, namely, a lack of real-time chemical sensing capability with sufficient spatial resolution. A Raman microscope was integrated with a custom bench-scale RO flow cell, outfitted with a long optical window. Given that scale progression on pressure-driven, crossflow filtration membranes is a function of axial position, the utilized experimental setup allowed for chemical detection of the scalant at downstream and upstream regions on the membrane using Raman spectroscopy. Crossflow filtration experiments were conducted, ensuring hydrodynamics reflective of more realistic RO operating conditions compared to dead-end filtration. Calcium carbonate was selected as a model scalant, which highlighted the Raman technique's ability to detect small crystals (<50 μm). The time evolution of the calcium carbonate Raman signal served as evidence of local progression of calcium carbonate scaling on RO membranes.

2. Materials and methods

Real-time, in-situ Raman data were collected for eight independent reverse osmosis experiments. The objective of each experiment was to demonstrate chemical detection of calcium carbonate scaling as well as compare the Raman data obtained from two different axial positions on the membrane (downstream vs upstream).

2.1. Scaling experiments

Undersaturated feed solutions were utilized to maintain scaling in the surface crystallization regime [37]. The bulk feed saturation index with respect to calcite was $SI_{Calcite} = \log_{10}(IAP/K_{sp}) \approx -0.6$, where IAP is the ionic activity product and K_{sp} is the solubility product constant [38]. Feed solutions were prepared by combining 8 L of deionized (DI) water with 1.51 g $NaHCO_3$ (2.25 mM) and 1.33 g $CaCl_2$ (1.5 mM). Prior to conducting scaling experiments, the reverse osmosis (RO) system was flushed for several hours with DI water until conductivity readings reached ≤1 μS/cm. Each membrane sample was soaked in a 50% solution of isopropanol for 30 min to remove preservatives. Afterwards, the membrane was compacted (~12–15 h) with a fresh reservoir of DI water to minimize compaction contributions to permeate flux decline during the scaling experiments. The same RO operating conditions were applied in both the compaction and scaling phases. A volumetric flow rate of 25 L/h (crossflow velocity of 3.0 cm/s) was selected such that the flow in the channel remained laminar, resulting in a Reynolds number of ~63 with respect to the channel height as the characteristic length [37]. For the selected feed temperature of 24°C and feed pressure of 1.03 MPa (150 psi), the initial permeate flux during scaling was 57.6 ± 6.3 L/m²/h, which underscores the variability in membrane performance and operating conditions among replicate scaling experiments (Table 1).

2.1.1. Reverse osmosis system

A bench-scale RO system was built with data acquisition capability to accommodate multi-day filtration tests (Fig. 1).

A custom-built plate-and-frame RO flow cell constructed from stainless steel featured a rectangular optical window with an area of 9.98 cm × 3.23 cm (length × width) that interfaced with the Raman microscope for scaling detection. The dimension of the optical window allowed for a range of Raman sensing locations along the axial length (feed-flow direction) of the membrane. The flow cell design included an inset glass window designed to provide a uniform channel height of 2 mm. The top plate housed the inlet feed and outlet retentate ports, and the bottom plate contained the permeate exit port, from which the permeate flux was measured using an in-line MEMS low-liquid flow sensor (SLF3S-1300, Sensirion); permeate was then subsequently returned to the active feed reservoir. The bottom plate also

Table 1
Summary of RO system operating parameters and permeate flux for scaling Tests 1–8

Test #	RO system operating parameters			Membrane performance (L/m²/h)		
	Crossflow velocity (cm/s)	Pressure (MPa)	Temperature (°C)	Initial flux during scaling	Mean flux during downstream detection	Mean flux during upstream detection
1	2.8 ± 0.0	1.057 ± 0.004	23.9 ± 0.1	58.6	55.6	50.5
2	2.8 ± 0.0	1.049 ± 0.005	23.7 ± 0.2	61.7	61.2	54.1
3	2.8 ± 0.1	1.050 ± 0.014	23.5 ± 0.1	59.7	59.7	50.7
4	3.0 ± 0.2	1.038 ± 0.007	24.7 ± 0.2	43.4	35.8	33.7
5	3.2 ± 0.1	1.062 ± 0.012	23.9 ± 0.2	55.6	51.4	45.5
6	2.9 ± 0.0	1.042 ± 0.003	22.3 ± 0.1	64.1	63.5	53.6
7	3.0 ± 0.0	1.073 ± 0.002	23.3 ± 0.3	60.5	59.8	50.0
8	2.8 ± 0.1	1.064 ± 0.007	23.7 ± 0.3	57.3	54.6	50.5

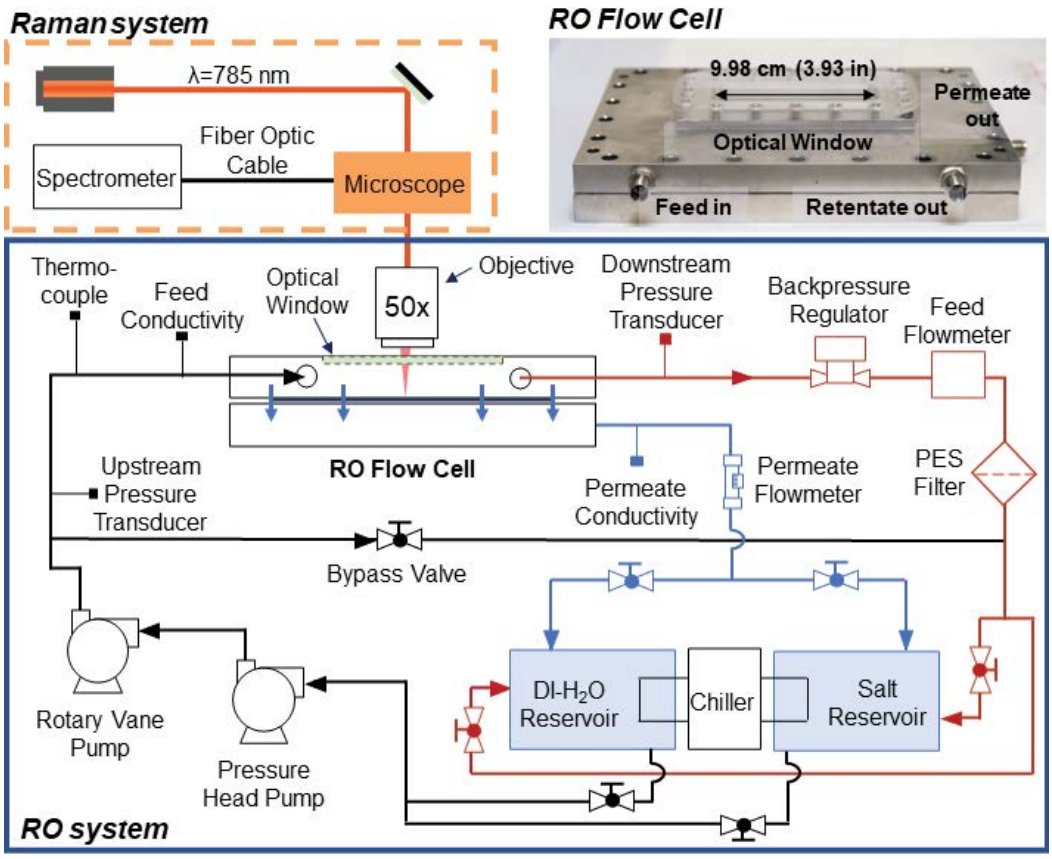

Fig. 1. Schematic of Raman system (dotted orange outline), reverse osmosis system (solid blue), and photograph of reverse osmosis flow cell pictured with protective optical window cover. The optical window has dimensions of 3.23 cm × 9.98 cm, resulting in 6.98 cm of axial travel for the ~3.0 cm-diameter, 50X microscope objective.

housed a steel mesh plate that provided structural support for the membrane during operation at a pressure of 1.03 MPa (150 psi). Membrane samples were cut from the same batch of thin-film composite reverse osmosis membranes (UTC-73HA, Toray), with each sample sized to an active membrane area of 17.5 cm × 12.5 cm (length × width).

Two feed tanks, one for DI water and the other for the prepared salt solution, were outfitted with feed intake valves and retentate return lines, allowing for RO operation in total-recycle mode and streamlined transitions between DI water and salt feeds. A thermocouple (TC-T-NPT-U-72, Omega) installed upstream of the flow cell monitored the temperature of the inlet feed stream. A U-tube style heat exchanger was submerged in both feed tanks and connected to a chiller (T257P, Thermotek) to maintain constant inlet feed stream temperatures during filtration.

Experimental feed temperature ranges for replicate tests are summarized in Table 1. In-line conductivity probes were used to measure the conductivity of the feed (EW-19500-65, Cole-Parmer) and permeate streams (EW-19500-64, Cole-Parmer). Pressure transducers (PX191-300GV5, Omega) installed upstream and downstream of the flow cell, monitored the feed channel pressure. A backpressure regulator (12-251B2-44AZ5-72, Neon) and a bypass valve (SS-1RS4, Swagelok) were used to manually set the applied feed pressure and volumetric flow rate at the start of all experiments, and a turbine flow meter (TFM-LP07, Dwyer) measured the feed volumetric flowrate. The ranges for experimental feed pressure and crossflow velocities (derived from volumetric flowrates) are also summarized in Table 1. All sensors were connected to a computer data acquisition system (USB-6001, National Instruments), except for the permeate flux sensor, which was connected to the computer via an Arduino board (Arduino Uno R3). A 0.2 μm PES filter (CCS-020-C1B, Advantec) was installed in the retentate line to filter any large particulates.

2.1.2. Raman data collection

The laser source employed was a narrow linewidth, 785-nm laser diode, and the beam was focused onto the sample using a 50X objective with ~27 mW of optical power incident on the sample (FPV785S, Thorlabs Inc). A 600 line/mm grating with a blaze at 1,000 nm provided a spectral dispersion of ~1 cm^{-1}/pixel. During each scaling experiment, all Raman spectra were acquired every 60 s with 10 s of integration time. All Raman data were preprocessed using the same procedures and parameters to avoid introducing artifacts [39]. Each spectrum was first baseline-corrected [40] to remove the fluorescent background signal, and cosmic rays were eliminated by linear interpolation. After baseline removal, all spectra were normalized by vector normalization to remove the effects of fluctuations in laser intensity and focus. Intensities of investigated Raman bands were expressed as ratios (%) to the most prominent RO membrane Raman band at 1,150 cm^{-1} (C–O–C stretching mode).

In each replicate scaling experiment, Raman detection was comprised of two parts, in which real-time Raman spectra were acquired downstream and upstream, in series (Fig. 2).

Raman spectral acquisition was initiated during the last ~30–60 min of DI water compaction, when no calcium carbonate crystals on the membrane are expected due to prior system cleaning. This expectation is supported by observation of relatively constant permeate flux, where minimal flux decline is attributed to continued effects of membrane compaction. When the feed is switched to the salt solution, supersaturated levels of solute ions at the membrane surface, due to concentration polarization [30,41,42], provide conditions necessary for scaling. Downstream detection began first (x = 12.2 cm) since early scaling crystals tend to form near the channel exit [5,28,41]. Raman detection of the scalant occurs when partial/full crystal dimensions overlap with the focal volume of the laser beam, causing an increase in the scalant Raman band intensity.

In both the literature [43,44] and the present work, the dominant calcium carbonate polymorph is calcite, whose strongest internal vibrational mode (V_1) has been reported to occur at a Raman shift of 1,086 cm^{-1} [45,46]. In the recorded Raman data, the maximum intensity for the calcite Raman band typically occurred at 1,086 cm^{-1}. Occasionally, maximum Raman intensities at 1,087 cm^{-1} were observed. The origin of the 1,087 cm^{-1} band was not certain, but a likely explanation is the use of a slightly deviated value for the excitation

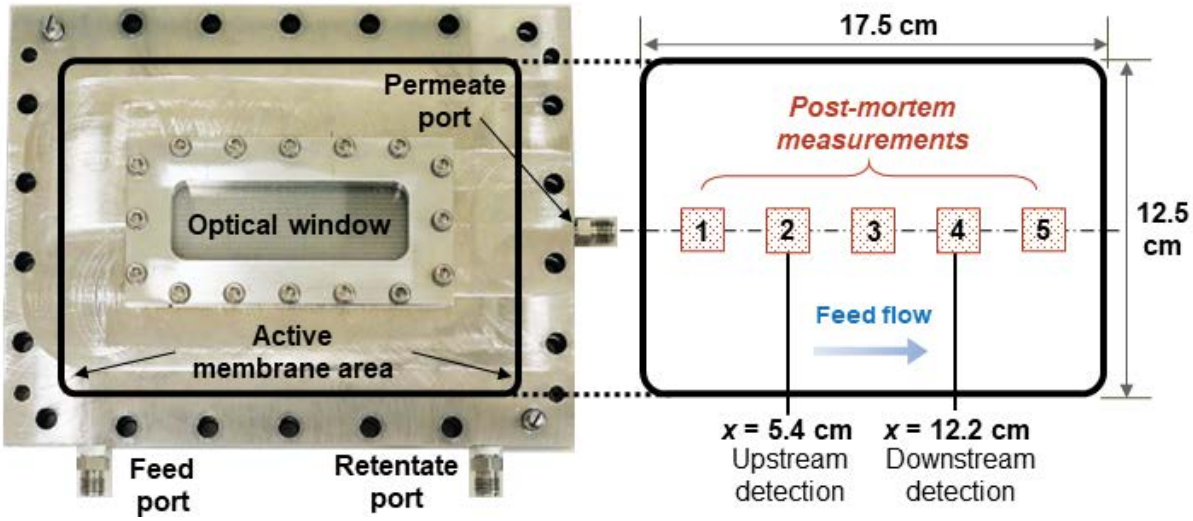

Fig. 2. The active membrane area is schematically represented on the bench-scale flow cell (pictured on the left). Downstream Raman detection at x = 12.2 cm is initiated first due to higher scaling propensity toward the channel exit. After completing downstream detection, the stage is moved to initiate upstream detection at x = 5.4 cm. To avoid edge effects, both downstream and upstream detection occurred at the center of the membrane, represented by the dotted centerline. The five square regions (1–5) represent membrane coupons that underwent post-mortem characterization, with the second and fourth squares encompassing the locations of upstream and downstream Raman detection, respectively.

laser line, which is used to convert wavelengths (nm) of Raman-scattered light to wavenumbers (cm^{-1}). A deviation of ~0.06 nm (i.e., the current pixel resolution) in the specified laser line would offset all measured wavenumbers by ~1 cm^{-1}. Another possibility is the presence of trace impurities in the calcite scaling crystals [47,48]. For the present study, the calcite Raman signal was defined as the average of the Raman intensities at 1,086–1,087 cm^{-1}, to allow for consistent processing of all Raman datasets. A spectral range of 500–1,500 cm^{-1} was specified for Tests 1–7, and for a final scaling test (Test 8), a spectral range of 100–1,200 cm^{-1} was specified to investigate proof-of-concept real-time detection of calcium carbonate polymorphs which exhibit distinct Raman bands at wavenumbers <400 cm^{-1}.

During membrane compaction, only the spectral bands of the RO membrane are represented in the Raman signal [36]. As calcite overlaps with the Raman sensing site during membrane scaling, the calcite Raman signal is convolved with the Raman signal of the RO membrane. Thus, the time-averaged Raman intensity of the 1,086 cm^{-1} Raman bands during membrane compaction is taken as a point of reference. A threshold value obtained at approximately three standard deviations above the reference signal served as the criterion for downstream Raman detection of calcite scale. Downstream detection (x = 12.2 cm in Fig. 2) was terminated and upstream detection (x = 5.4 cm) initiated when the calcite Raman signal exceeded the defined threshold value.

Since initial upstream detection began at a later stage of the scaling experiment, compared to initial downstream detection, there is a possibility of pre-existing scaling crystals near or within the upstream laser focal volume. Thus, a secondary detection threshold value was established, defined as three standard deviations above the mean calcite Raman signal during the first 10 min of upstream detection. The secondary threshold value was used as criterion for termination of each scaling experiment. Additionally, the secondary threshold value enabled collection of sufficient data for determination of the time evolution of the upstream calcite Raman signal, discussed in detail in the following section. The presented two-part Raman detection scheme used in this work allows for the investigation of earlier/downstream and later/upstream calcite scaling progression.

2.1.3. Time evolution of calcite Raman signals

In the present study, we report on the relationship between the time evolution of the calcite Raman signal and local progression of calcite scaling. Fig. 3 shows a representative dataset comprised of real-time calcite Raman signals and permeate flux as a function of time, with the time evolution of the calcite Raman signal, that is, the slope, represented schematically. The slope is given by Eq. (1) where RI(t_f) and RI(t_i) are the calcite Raman intensity at the final and initial timestamp (t_f and t_i, respectively) of the calcite Raman signal's time-evolution period.

$$m = \frac{\mathrm{RI}\left(t_f\right) - \mathrm{RI}\left(t_i\right)}{t_f - t_i} \tag{1}$$

The time evolution of the calcite Raman signal during compaction is expected to be zero [Eq. (2)] since Raman spectra acquired during this period reflect Raman bands of only the RO membrane, whose chemical composition is assumed to remain constant.

$$m\left(t_f = t_{c2}, t_i = t_{c1}\right) \approx 0 \tag{2}$$

When the feed is switched to the salt solution and scaling initiates at the detection site, the calcite Raman signal exhibits a steady increase. The downstream and upstream Raman time evolutions of calcite were obtained by identifying the periods during which the mean and slope of the calcite Raman signal experienced an abrupt change.

2.2. Post-mortem characterization

The measured real-time data were complemented by post-mortem characterization of membrane samples from Tests 1–8. Scaled membranes were cut into 2 cm × 2 cm coupons from five locations along the direction of feed flow (Fig. 2). Gravimetric analysis was conducted by weighing the membrane coupons using a microbalance and measuring the dimensions of the coupons using a digital caliper. SEM (scanning electron microscope) images of the membrane coupons provided length-scale estimates of the calcium carbonate crystals. These estimates were obtained using image processing packages available in Fiji [49]. The heights of calcium carbonate crystals were measured using a laser interferometer. For SEM imaging and laser interferometry, membrane coupons were coated with ~2 nm of platinum prior to analysis.

2.3. Estimation of local saturation indices

Comparison of the time evolution of calcite Raman signals across replicate scaling experiments requires

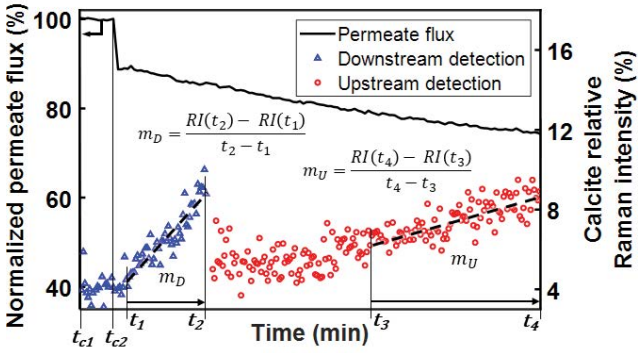

Fig. 3. Representative dataset from a scaling experiment, showing normalized permeate flux and calcite relative Raman intensity over time. The time evolution of the calcite Raman signal is indicated by the dotted lines and calculated for time periods defined by the following timestamps ($t_{\#}$): t_{c1}: Start of membrane compaction phase; t_{c2}: End of membrane compaction phase; t_1: Start of downstream Raman time evolution; t_2: End of downstream Raman time evolution; t_3: Start of upstream Raman time evolution; t_4: End of Raman upstream time evolution.

careful consideration of the inherent variability in membrane performance, RO system operating parameters, and spatiotemporal dependencies of local scaling conditions. Estimation of local saturation indices (SI) at the membrane surface can be used to streamline this variability, by serving as a comparison metric that accounts for different axial position and experimental conditions which, in turn, result in different concentration levels at the membrane wall. The membrane wall concentration profile is often expressed using the concentration polarization modulus (CP) [50], which normalizes the solute ion concentration at the membrane wall (C_m) to that in the bulk feed (C_b). This concentration polarization modulus is represented by an analytical solution derived from classical one-dimensional film theory [28,51] (Eq. 3).

$$\mathrm{CP} = \frac{C_m - C_p}{C_b - C_p} = \frac{\Delta\pi_m}{\Delta\pi_b} = \left(1 - R\right) + R \cdot \exp\left(\frac{J_v}{k_m}\right) \tag{3}$$

Salt rejection (R) was assumed to be 1 (complete solute rejection). Consequently, permeate concentration (C_p) was approximated to be 0, which corresponded to a lower limit estimate of the CP modulus. $\Delta\pi_m$ and $\Delta\pi_b$ are the osmotic pressures at the membrane wall (feed side) and bulk solution, respectively; J_v is the local permeate flux and $k_m = D/\delta$ is the local mass-transfer coefficient, which is a ratio of the salt diffusion coefficient (D) and the boundary layer thickness (δ). The permeate flux is given by Eq. (4) [52] which relates permeability of the membrane (L_p), applied feed pressure (P), and osmotic pressure at the membrane wall.

$$J_v = L_p\left(P - \Delta\pi_m\right) \tag{4}$$

In Eq. (5), the Sherwood number (Sh) obtained from the Graetz solution [50–52] is used to couple fluid flow with mass transfer in a thin rectangular channel, as a function of axial position (x).

$$\mathrm{Sh} = \frac{k_m d}{D} = 1.85\left(\mathrm{Re}\cdot\mathrm{Sc}\cdot\frac{2d}{x}\right)^{1/3} \tag{5}$$

The Sherwood number considers the flow cell geometry (hydraulic diameter, d); the Reynolds number (Re = Ud/ν), which includes the crossflow velocity (U) and kinematic viscosity of the feed solution (ν); as well as the Schmidt number (Sc = ν/D) which describes solute properties. The concentration profile at the membrane wall was estimated by computing the Sherwood number at discretized values of axial position [51]. A boundary condition of CP(x = 0 cm) = 1 was assumed (i.e., no concentration polarization) because the permeate flux at the channel entrance is assumed to be zero. Fig. 4 presents the computed CP modulus, boundary layer thickness, and permeate flux profiles as a function of nondimensional axial position (x/L, L = 17.5 cm) for Tests 1–8, using experimentally determined inputs of mean crossflow velocity, pressure, temperature, and initial permeate flux values (J_{v0}) (Table 1).

According to the computed CP modulus and boundary layer thickness profile for each test, both the concentration of scaling ions and the boundary layer thickness are observed to increase with increasing axial position ($x/L \rightarrow 1$). Additionally, the variability in scaling conditions across Tests 1–8 is depicted by the distinct CP modulus and permeate flux profiles of each test.

For the estimation of the local saturation index, the CP modulus was computed using the known value of the bulk feed concentration and estimates of the CP modulus at the upstream (x = 5.4 cm) and downstream (x = 12.2 cm) Raman detection regions. For simplicity, only major scaling ions (Ca^{2+}, CO_3^{2-}) were considered in the estimation of saturation indices with respect to calcite ($SI_{calcite}$), using PHREEQC Interactive 3.7.0 software [38].

3. Results and discussion

3.1. Raman monitoring of the RO membrane

The Raman spectrum of the RO membrane exhibits Raman bands at 740, 792, 1,073, 1,110, and 1,149 cm^{-1}, which were identified as belonging to the polysulfone layer of the RO membrane in previous work [36]. In the present study, the thin-film composite polysulfone/polyamide (PSF/PA) layer of a virgin sample of the RO membrane was peeled off using masking tape to reveal the nonwoven polyethylene terephthalate (PET) support layer. Each

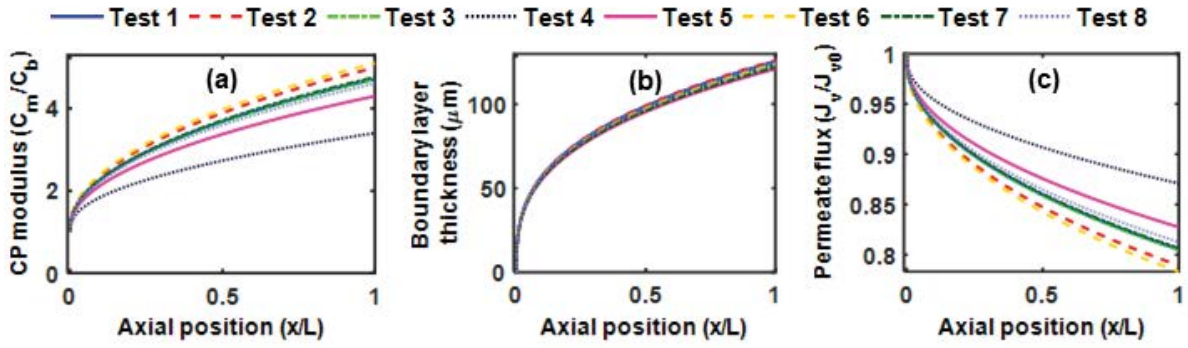

Fig. 4. (a) The concentration polarization (CP) modulus, (b) boundary layer thickness, and (c) normalized permeate flux was computed as a function of axial position [51]. Concentration at the membrane wall increases with increasing axial position [50].

layer was fixed on a glass slide and analyzed in vitro using the Raman microscope (Fig. 5). The PET Raman bands at 281, 303, 634, and 861 cm^{-1} [53] were also observed in the real-time Raman spectrum of the RO membrane during compaction. Raman observation of support layers is possible, depending on the level of defocus of the Raman laser beam [54]. In the subsequent discussion of calcium carbonate Raman data, it is important to note the influence of the PET support layer given that calcium carbonate polymorphs exhibit Raman bands that may overlap with those of the PET layer (e.g., 281 and 301 cm^{-1} for the calcite and vaterite polymorphs, respectively).

The aim of the present work was to attribute an increase in the calcite Raman signal to a volumetric increase in scaling crystals within the Raman sampling volume, or focal volume. This is due to the fact that a molecule's Raman signal intensity is proportional to the number of Raman scattering molecules within the focal volume [55,56]. However, there are other confounding variables that could cause an increase in the Raman signal intensity, such as changes in the laser beam focus or in the surface roughness of the Raman-sampled area. Consequently, when the Raman sampling area surpasses the dimensions of the overlapping scaling crystals, the contributing effects of the confounding variables on Raman signal intensity will decrease. Conversely, when the Raman sampling area is much smaller than overlapping crystal dimensions, resulting in a potentially overfilled laser focal volume, possible effects of the confounding variables must be considered.

Therefore, it was necessary to first establish whether the Raman sampling area was sufficient for the study of calcium carbonate scaling progression by investigating whether the laser focal volume was being overfilled by calcite crystals. The basis for this analysis was that a decrease in the real-time RO membrane Raman signal (i.e., obstruction of the membrane substrate) could be considered analogous to an overfilled laser focal volume. The Raman band at ~792 cm^{-1} (out-of-plane bending of the C–H bond in the benzene ring) was selected as a representative RO membrane Raman signal to avoid including potential Raman signal contributions from calcium carbonate (~1,080–1,090 cm^{-1}). An additional DI water feed experiment was conducted using the same preconditioning and Raman spectral acquisition procedures described for the other scaling experiments. Raman data for the DI feed experiment and a representative calcium carbonate scaling experiment are shown in Fig. 6. For the DI feed experiment (Fig. 6a), a slight initial decrease in the membrane Raman signal (~4%) is detected at the start of both downstream and upstream observation. Despite background removal in data preprocessing, this is likely due to decreases in the fluorescent background over time, which was consistently observed in the last 30–60 min of compaction in the other scaling experiments. Overall, no consistent trends are observed in the time evolution of the 792 cm^{-1} Raman signal during the DI feed experiment, serving as a standard of comparison and confirming the absence of false positive calcium carbonate detection [34]. For a representative scaling experiment (Fig. 6b), no discernable changes in the membrane Raman signal were observed, even while the calcite Raman signal consistently increased over time.

The relatively steady 792 cm^{-1} band Raman signal over the duration of the scaling experiment, serves as evidence that the increase in the calcite Raman signal was due to a gradual growth of calcite scale on the membrane surface, rather than the misleading effect of a length-scale mismatch between the Raman sampling area and scaling crystals.

3.1.1. Scaling crystal characteristic length

Due to the previously noted importance of length-scale matching between the Raman sampling area and scaling crystals, it was necessary to identify a critical length-scale in the current membrane system. We refer to this critical

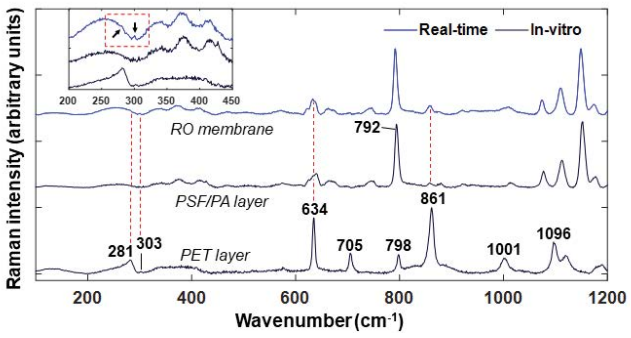

Fig. 5. In vitro Raman spectra of the polyethylene terephthalate (PET) non-woven support layer and the polysulfone support/polyamide (PSF/PA) layer compared to a real-time Raman spectrum of the reverse osmosis membrane during compaction in Test 8.

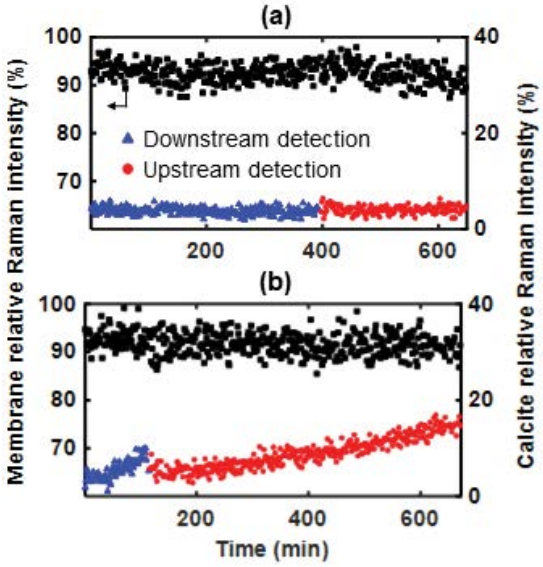

Fig. 6. No sustained trends are observed for the 792 cm^{-1} membrane Raman signal from the (a) deionized (DI) water feed experiment and (b) representative calcium carbonate scaling experiment. The calcium carbonate Raman signal remained constant for the DI water feed experiment and consistently increased for the calcium carbonate scaling experiment.

length-scale as the crystal characteristic length, which was defined as the longest measured diagonal of a calcite crystal face. SEM image analysis of representative scaled membrane samples showed crystal characteristic lengths predominantly ranging from 20–50 μm. For example, the double arrow in Fig. 7b shows a crystal characteristic length of ~30 μm. For the same membrane samples, laser interferometry measurements indicated representative crystal heights of ~10 μm.

Overall, the characteristic length range of the calcite crystals was somewhat larger than the laser beam spot size of ~3 μm (FWHM, full width at half maximum) whereas the crystal heights were similar to the laser beam depth of focus (~9 μm). Given that the crystal characteristic length measurements were taken from samples that underwent 9–30 h of scaling and that Raman detection of calcium carbonate occurred as early as 30–60 min into the scaling experiment, calcium carbonate crystals were likely much smaller during the initial stages of scaling. This is substantiated by post-mortem observation of calcite characteristic lengths as small as ~5 μm (Fig. 7b). Moreover, Raman detection of calcium carbonate scaling crystals <50 μm in characteristic length demonstrates the high spatial resolution of the technique.

3.2. Raman monitoring of calcium carbonate scaling

3.2.1. Calcium carbonate polymorphs

Calcium carbonate is an inorganic crystal comprised of calcium and carbonate ions. Raman bands of calcium carbonate due to its internal vibration modes ($V_{1...n}$) are attributed to vibrations within the ionic species. Additionally, these ionic species can be arranged into different lattice structures, resulting in three main polymorphs that exhibit different Raman bands arising from lattice vibrations (<400 cm^{-1}). For example, aragonite and vaterite, two other polymorphs of calcium carbonate, with V_1 vibrational modes occurring at 1,085 cm^{-1}, and 1,090 and 1,075 cm^{-1} respectively [45,46], have also been observed in scaling studies [44,58]. However, to verify the exact calcium carbonate polymorph, Raman bands attributed to lattice structure are typically measured. For this reason, in Test 8 (Fig. 8), Raman data were collected with a spectral range of 100–1,200 cm^{-1} to investigate whether it was possible to distinguish calcium carbonate polymorphs in real time. During both downstream and upstream detection, the 1,087 cm^{-1} band was observed, suggesting Raman detection of a calcite polymorph. As for the observed Raman band at 281 cm^{-1}, due to its low signal-to-noise ratio, it is difficult to confirm whether the band is due to lattice vibration of calcite [45] or the PET layer of the membrane.

SEM images (Fig. 7) confirmed a majority of rhombic calcite polymorphs and a few hexagonal plate vaterite crystals. Given the dominance of calcite, detection of other polymorphs did not occur in real-time. Thus, polymorph detection was carried out via post-mortem Raman measurements of scaled membrane samples. Raman bands at 301, 332, 1,075, and 1,090 cm^{-1} [45,46] confirmed the presence of vaterite polymorphs on the Test 8 membrane sample. However, the challenge of weak signal-to-noise ratios still remained, due to the less-ordered crystalline form of vaterite compared to that of calcite [59]. Despite these limitations, the present work indicates the potential of the technique to distinguish polymorphs of calcium carbonate, which is critical in the investigation of scaling dynamics of single and multiple component feed solutions. Depending on the properties of the feed solution such as ionic strength, ratio of scaling ion concentrations, and the presence of additional components in the feed water [60,61], the pathways to $CaCO_3$ crystallization are broad, resulting in initial polymorphs which can evolve over time into other polymorphs. Additionally, since co-precipitation is a common occurrence in industrial water systems [62], crystallization pathways can be even

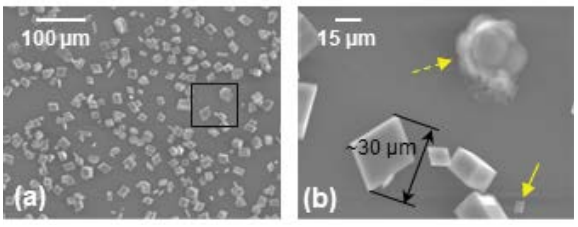

Fig. 7. SEM images of representative calcium carbonate scaling crystals with characteristic lengths of ~20–50 μm (a) from the region of upstream Raman observation (x = 5.4 cm). Higher magnification image of the region indicated by the rectangle is shown in (b), where the double arrow depicts an example of a characteristic length measurement. A small calcite crystal with a characteristic length of ~5 μm (yellow solid arrow) and a hexagonal-plate vaterite [57] polymorph (yellow dashed arrow) are also observed.

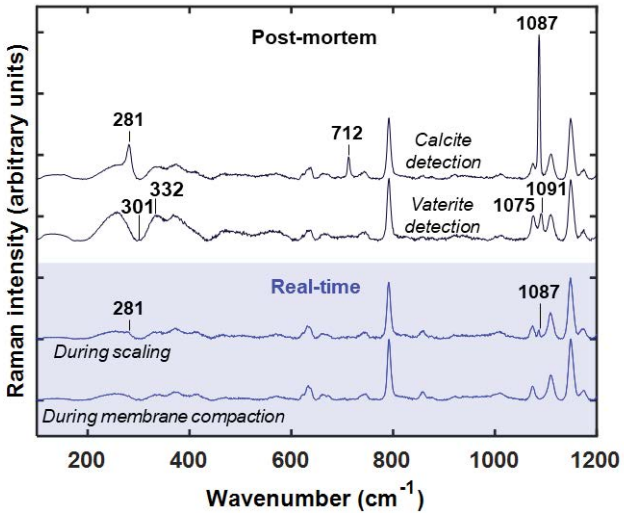

Fig. 8. Representative real-time vs post-mortem Raman spectra. A real-time Raman spectrum of the reverse osmosis membrane during membrane compaction (Test 8) shows an absence of calcium carbonate Raman signals. A Raman spectrum acquired during scaling suggests detection of a calcite polymorph due to the appearance of the 1,087 and 281 cm^{-1} bands. Post-mortem Raman spectra of Test 8's scaled membrane suggest the presence of the vaterite and calcite polymorphs, with lattice Raman bands at 301, 332, and 281 cm^{-1}, respectively.

further confounded. The initial results presented here suggest that such complexities can be studied in real-time with improvement of Raman signal-to-noise ratios.

3.2.2. Local calcite scaling progression

Metrics of solute supersaturation at the membrane wall are usually reported in bench-scale scaling studies because scaling rates are related to supersaturation levels [6,14,37,63]. According to classical nucleation theory [64–66], crystallization is comprised of nucleation and growth mechanisms. Either homogenous or heterogeneous crystal nucleation can occur when clusters of scaling ions aggregate to a stable, critical size. The heterogeneous nucleation mechanism is likely favored in the present membrane system, considering that heterogenous nucleation is most commonly reported for RO systems [12,67,68] and homogenous nucleation only occurs at extremely high levels of supersaturation [68,69]. Once stable nuclei are established, their continued growth depends on the degree of supersaturation, where growth rate increases with increasing supersaturation [22,65]. If the increase in the calcite Raman signal over time is attributed to the local volumetric increase of calcium carbonate scale at the detection site, it is reasonable to expect greater magnitudes of the calcite Raman signal time evolution, m, for greater local supersaturation levels. A summary of the time evolution of calcite Raman signals is presented in Fig. 9.

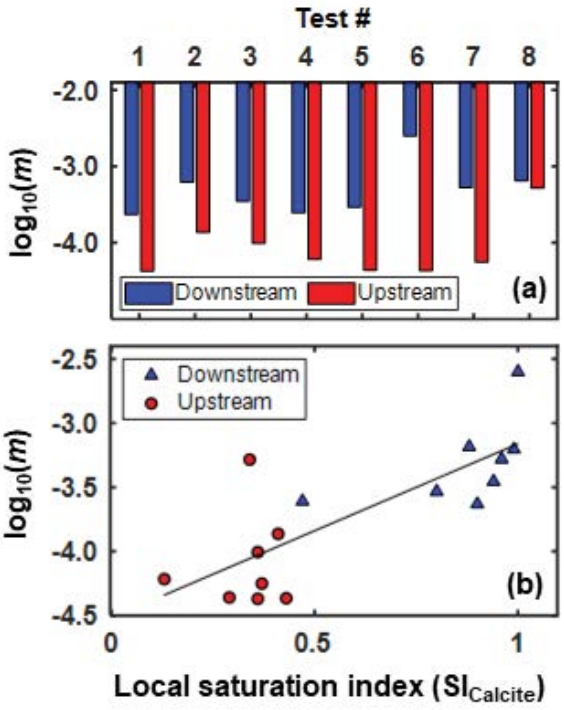

Fig. 9. (a) The time evolution of the calcite Raman signal (y-axis) is summarized for Tests 1–8 (top x-axis). For each test, downstream m values were found to be consistently greater than upstream counterparts by about an order of magnitude. (b) The time evolution of the calcite Raman signal evidenced a statistically significant dependence on the local saturation index; fitted regression line (black) with $p < 0.001$.

In Fig. 9a, downstream m values were found to be consistently greater than upstream counterparts by about an order of magnitude. This can be explained by boundary layer theory which describes higher concentrations of solute ions at the downstream membrane wall, causing greater scaling propensity in this region. This result was predicted by the computed CP modulus profiles and supported by post-mortem gravimetric analysis (Fig. 10), which showed a clear increase in calcium carbonate mass per area with increasing axial position.

The x-axis error bars in Fig. 10 capture the axial dimension of the membrane coupons (2 cm). The y-axis error bars are large due to variability in scale coverage between Tests 1–8, which can be attributed to some variation in initial permeate flux, scaling duration, and operating conditions. Despite the significant variation in scale density among the replicate tests, more scale is observed downstream as compared to upstream regions, supporting the results of Fig. 9a.

In Fig. 9b, m values are plotted for downstream and upstream observation from the eight replicate $CaCO_3$ scaling tests, resulting in a total of 16 data points. Generally, the expected trend is observed across all scaling experiments, such that there is a statistically significant dependence of m on local $SI_{calcite}$ values ($p < 0.001$). Strong literature evidence of scaling dependence on supersaturation levels [65,69–71] supports the observed relationship between m and $SI_{calcite}$. Changes in Raman signals over time appear to be a useful metric for comparisons of local scaling progression within a membrane sample (i.e., downstream vs upstream) and across different membrane samples.

4. Conclusions

Real-time chemical sensing is critical in the overall optimization of reverse osmosis (RO) desalination, given the highly chemistry-specific nature of antiscaling and cleaning protocols. In the present work, Raman spectroscopy was used to chemically identify and monitor the progression

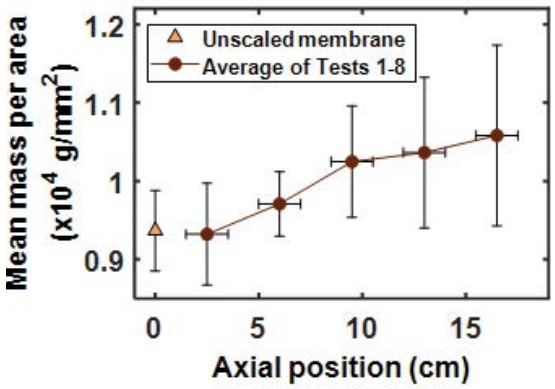

Fig. 10. Post-mortem gravimetric analysis. An increase in mean calcium carbonate mass per area with increasing axial position confirms the presence of higher supersaturation levels towards the downstream region ($x \rightarrow 17.5$ cm). The y-axis error bars are large due to significant variation in scale coverage between Tests 1–8. The x-axis error bars represent the width of each membrane coupon (2 cm).

of calcium carbonate scaling on RO membranes. A bench-scale plate-and-frame RO flow cell outfitted with a long optical window enabled real-time detection of calcium carbonate scaling at sequential downstream and upstream axial positions. The most commonly observed Raman band occurred at 1,086 cm^{-1}, which belongs to the calcite polymorph. Post-mortem SEM images showed that most crystals exhibited a rhombohedral crystal habit, characteristic of the calcite polymorph.

The time evolution of the calcite Raman signal was represented by m, defined as the slope of the calcite relative Raman peak intensity with respect to time. It was hypothesized that the magnitude of m could be related to local volumetric increases of calcium carbonate scale at the site of Raman detection. For each replicate scaling experiment, it was observed that the time evolution of the downstream calcite Raman signal consistently exceeded its upstream counterpart. Additionally, downstream and upstream values of m were compared to corresponding values of local saturation indices, computed using inputs of mean experimental operating conditions. This comparison revealed that the time evolution of calcite Raman signals (m) had a statistically significant dependence on local estimates of saturation indices whereby increasing local saturation indices generally resulted in increased values of m. These results suggested that the time evolution of calcite Raman signals could serve as a useful measure of scaling progression within a membrane sample (i.e., downstream vs upstream) and across different membrane samples. Post-mortem gravimetric measurements revealed greater values of mean mass per area at the downstream axial position, which corresponded to greater computed values of local saturation index as compared to that of the upstream axial position. This result further supported the statistically significant dependence of m on local saturation indices.

Spectral data generally require careful interpretation due to the presence of potential artifacts. Thus, progression of the RO membrane band at 792 cm^{-1} was also studied because any changes in the laser focal plane or obstruction of the membrane substrate would affect the Raman spectrum of the substrate. The RO membrane Raman signal remained relatively constant throughout the scaling experiment despite a steady increase in the calcite Raman signal. This result suggests that the steady increase in the calcite Raman signal was caused by slow volumetric growth of calcite crystals which remained small enough to leave the interrogated membrane substrate undisturbed. This was further supported by post-mortem SEM imaging of the scaled membranes which showed the presence of small scaling crystals (<50 μm). Therefore, matching the characteristic lengths of the Raman sampling area and crystallite was identified as an important aspect of the presented Raman methodology. The SEM images also revealed that there were scale-free regions on the membrane. If the Raman sampling area coincided with a scale-free region, but crystals were adjacently present, a false negative detection result would have been observed. However, in all eight replicate scaling experiments, calcite scale was successfully detected at both downstream and upstream axial positions.

The demonstrated ability to study high-resolution, single-component scaling progression with chemical identification is an important step towards applying the in-situ Raman monitoring technique in expanded studies of other relevant scalant chemistries and mixed salt scaling. This information could be used to develop more effective scale mitigation strategies and improve predictive scaling models, ultimately enabling further optimization of RO desalination.

Acknowledgements

The authors gratefully acknowledge the support of this work by NSF (National Science Foundation) through award CBET 1826542. The authors also acknowledge support for the early stages of this work from the Membrane Science, Engineering and Technology Center (NSF IUCRC Award IIP 1624602) at the University of Colorado Boulder. The authors also appreciate the assistance of flow cell fabrication provided by Dragan Mejic, Dr. Emily Gibson at the University of Colorado Anschutz for use of the spectrometer and detector, and Dr. Colin Ingram at Princeton Instruments for technical guidance and access to software and instrumentation.

Symbols

C	Salt concentration
CP	Concentration polarization modulus
D	Salt coefficient of diffusion
d	Hydraulic diameter
δ	Boundary layer thickness
J_v	Permeate flux
k_m	Mass transfer coefficient
K_{sp}	Solubility product constant
L	Axial membrane length
L_p	Membrane permeability
m	Time evolution of calcite Raman signal (i.e., slope)
P	Applied feed pressure
p	p-value (statistics)
$\Delta\pi$	Osmotic pressure
R	Salt rejection
t_i	Initial timestamp of calcite Raman signal time evolution
t_f	Final timestamp of calcite Raman signal time evolution
U	Feed crossflow velocity
ν	Kinematic viscosity
$V_{1\ldots n}$	Raman vibrational modes
x	Axial position

Subscripts

b	Bulk feed
c	Compaction
D	Downstream
m	Membrane wall
p	Permeate
U	Upstream

Abbreviations

DI	Deionized

EIS	Electrical Impedance Spectroscopy
FWHM	Full Width at Half Maximum
IAP	Ionic Activity Product
lpmm	Lines per mm
PA	Polyamide
PES	Polyethersulfone
PET	Polyethylene terephthalate
PSF	Polysulfone
Re	Reynolds number
RI	Raman Intensity
RO	Reverse Osmosis
Sc	Schmidt number
Sh	Sherwood number
$SI_{calcite}$	Saturation index with respect to calcite
UF	Ultrafiltration
UTDR	Ultrasonic Time-Domain Reflectometry
VO	Visual Observation

References

[1] R. Singh, Water and Membrane Treatment, in: Membr. Technol. Eng. Water Purif., Elsevier, 2015, pp. 81–178.

[2] E.P. Chan, A.P. Young, J.-H. Lee, C.M. Stafford, Swelling of ultrathin molecular layer-by-layer polyamide water desalination membranes, J. Polym. Sci., Part B: Polym. Phys., 51 (2013) 1647–1655.

[3] Z. Amjad, K.D. Demadis, Mineral Scales and Deposits: Scientific and Technological Approaches, Elsevier, Oxford, The Netherlands, 2015.

[4] A.G. Pervov, G.Y. Rudakova, Development of New Phosphonic Acid Based Scale Inhibitors and Evaluation of Their Performance in RO Applications, Z. Amjad, Ed., Miner. Scale Form. Inhib., Springer US, Boston, MA, 1995, pp. 111–120.

[5] W.-Y. Shih, A. Rahardianto, R.-W. Lee, Y. Cohen, Morphometric characterization of calcium sulfate dihydrate (gypsum) scale on reverse osmosis membranes, J. Membr. Sci., 252 (2005) 253–263.

[6] A. Rahardianto, B.C. McCool, Y. Cohen, Reverse osmosis desalting of inland brackish water of high gypsum scaling propensity: kinetics and mitigation of membrane mineral scaling, Environ. Sci. Technol., 42 (2008) 4292–4297.

[7] J.C. Chen, Q. Li, M. Elimelech, In situ monitoring techniques for concentration polarization and fouling phenomena in membrane filtration, Adv. Colloid Interface Sci., 107 (2004) 83–108.

[8] L.N. Sim, J. Gu, H.G.L. Coster, A.G. Fane, Quantitative determination of the electrical properties of RO membranes during fouling and cleaning processes using electrical impedance spectroscopy, Desalination, 379 (2016) 126–136.

[9] M. Kögler, B. Zhang, L. Cui, Y. Shi, M. Yliperttula, T. Laaksonen, T. Viitala, K. Zhang, Real-time Raman based approach for identification of biofouling, Sens. Actuators, B, 230 (2016) 411–421.

[10] T. Virtanen, S.-P. Reinikainen, M. Kögler, M. Mänttäri, T. Viitala, M. Kallioinen, Real-time fouling monitoring with Raman spectroscopy, J. Membr. Sci., 525 (2017) 312–319.

[11] J. Li, D.K. Hallbauer, R.D. Sanderson, Direct monitoring of membrane fouling and cleaning during ultrafiltration using a non-invasive ultrasonic technique, J. Membr. Sci., 215 (2003) 33–52.

[12] A.P. Mairal, A.R. Greenberg, W.B. Krantz, Investigation of membrane fouling and cleaning using ultrasonic time-domain reflectometry, Desalination, 130 (2000) 45–60.

[13] S.A. Creber, J.S. Vrouwenvelder, M.C.M. van Loosdrecht, M.L. Johns, Chemical cleaning of biofouling in reverse osmosis membranes evaluated using magnetic resonance imaging, J. Membr. Sci., 362 (2010) 202–210.

[14] M. Uchymiak, A. Rahardianto, E. Lyster, J. Glater, Y. Cohen, A novel RO ex situ scale observation detector (EXSOD) for mineral scale characterization and early detection, J. Membr. Sci., 291 (2007) 86–95.

[15] J. Cen, M. Vukas, G. Barton, J. Kavanagh, H.G.L. Coster, Real time fouling monitoring with electrical impedance spectroscopy, J. Membr. Sci., 484 (2015) 133–139.

[16] M. Amin Saad, Early discovery of RO membrane fouling and real-time monitoring of plant performance for optimizing cost of water, Desalination, 165 (2004) 183–191.

[17] X. Lu, E. Kujundzic, G. Mizrahi, J. Wang, K. Cobry, M. Peterson, J. Gilron, A.R. Greenberg, Ultrasonic sensor control of flow reversal in RO desalination—Part 1: Mitigation of calcium sulfate scaling, J. Membr. Sci., 419–420 (2012) 20–32.

[18] A. Antony, J.H. Low, S. Gray, A.E. Childress, P. Le-Clech, G. Leslie, Scale formation and control in high pressure membrane water treatment systems: a review, J. Membr. Sci., 383 (2011) 1–16.

[19] A. Rahardianto, W.-Y. Shih, R.-W. Lee, Y. Cohen, Diagnostic characterization of gypsum scale formation and control in RO membrane desalination of brackish water, J. Membr. Sci., 279 (2006) 655–668.

[20] A.R. Bartman, E. Lyster, R. Rallo, P.D. Christofides, Y. Cohen, Mineral scale monitoring for reverse osmosis desalination via real-time membrane surface image analysis, Desalination, 273 (2011) 64–71.

[21] J. Thompson, A. Rahardianto, H. Gu, M. Uchymiak, A. Bartman, M. Hedrick, D. Lara, J. Cooper, J. Faria, P.D. Christofides, Y. Cohen, Rapid field assessment of RO desalination of brackish agricultural drainage water, Water Res., 47 (2013) 2649–2660.

[22] J. Thompson, N. Lin, E. Lyster, R. Arbel, T. Knoell, J. Gilron, Y. Cohen, RO membrane mineral scaling in the presence of a biofilm, J. Membr. Sci., 415–416 (2012) 181–191.

[23] A.J. Karabelas, M. Kostoglou, S.T. Mitrouli, Incipient crystallization of sparingly soluble salts on membrane surfaces: the case of dead-end filtration with no agitation, Desalination, 273 (2011) 105–117.

[24] J.-X. Li, R.D. Sanderson, G.Y. Chai, A focused ultrasonic sensor for in situ detection of protein fouling on tubular ultrafiltration membranes, Sens. Actuators, B, 114 (2006) 182–191.

[25] J. Liu, J. Li, X. Chen, Y. Zhang, Monitoring of polymeric membrane fouling in hollow fiber module using ultrasonic nondestructive testing, Trans. Nonferrous Met. Soc. China, 16 (2006) s845–s848.

[26] J.M. Kavanagh, S. Hussain, T.C. Chilcott, H.G.L. Coster, Fouling of reverse osmosis membranes using electrical impedance spectroscopy: measurements and simulations, Desalination, 236 (2009) 187–193.

[27] A. Antony, T. Chilcott, H. Coster, G. Leslie, In situ structural and functional characterization of reverse osmosis membranes using electrical impedance spectroscopy, J. Membr. Sci., 425–426 (2013) 89–97.

[28] P.L.T. Brian, Concentration polarization in reverse osmosis desalination with variable flux and incomplete salt rejection, Ind. Eng. Chem. Fundam., 4 (1965) 439–445.

[29] M.Y. Ashfaq, M.A. Al-Ghouti, D.A. Da'na, H. Qiblawey, N. Zouari, Effect of concentration of calcium and sulfate ions on gypsum scaling of reverse osmosis membrane, mechanistic study, J. Mater. Res. Technol., 9 (2020) 13459–13473.

[30] Z. Zhang, V.M. Bright, A.R. Greenberg, Use of capacitive microsensors and ultrasonic time-domain reflectometry for in-situ quantification of concentration polarization and membrane fouling in pressure-driven membrane filtration, Sens. Actuators, B, 117 (2006) 323–331.

[31] R.L. McCreery, Raman Microscopy and Imaging - Raman Spectroscopy for Chemical Analysis - Wiley Online Library, (n.d.).

[32] D.J. Gardiner, H.J. Bowley, Eds., Practical Raman spectroscopy: With 11 Tables, Springer, Berlin Heidelberg, 1989.

[33] T. Virtanen, P. Parkkila, A. Koivuniemi, J. Lahti, T. Viitala, M. Kallioinen, M. Mänttäri, A. Bunker, Characterization of membrane–foulant interactions with novel combination of Raman spectroscopy, surface plasmon resonance and molecular dynamics simulation, Sep. Purif. Technol., 205 (2018) 263–272.

[34] O.D. Supekar, D.J. Park, A.R. Greenberg, J.T. Gopinath, V.M. Bright, Real-time detection of early-stage calcium sulfate and calcium carbonate scaling using Raman spectroscopy, J. Membr. Sci., (2019) 117603.
[35] O.D. Supekar, D.J. Park, A.R. Greenberg, J.T. Gopinath, V.M. Bright, Real-time detection of early-stage calcium sulfate and calcium carbonate scaling using Raman spectroscopy, J. Membr. Sci., 596 (2020) 117603.
[36] D.J. Park, O.D. Supekar, A.R. Greenberg, J.T. Gopinath, V.M. Bright, Real-time monitoring of calcium sulfate scale removal from RO desalination membranes using Raman spectroscopy, Desalination, 497 (2021) 114736.
[37] M. Uchymiak, E. Lyster, J. Glater, Y. Cohen, Kinetics of gypsum crystal growth on a reverse osmosis membrane, J. Membr. Sci., 314 (2008) 163–172.
[38] D.L. Parkhurst, User's Guide to PHREEQC, A Computer Program for Speciation, Reaction-Path, Advective-Transport, and Inverse Geochemical Calculations, U.S. Geological Survey, Reston, VA, 1995.
[39] S. Guo, J. Popp, T. Bocklitz, Chemometric analysis in Raman spectroscopy from experimental design to machine learning–based modeling, Nat. Protoc., 16 (2021) 5426–5459.
[40] V. Mazet, C. Carteret, D. Brie, J. Idier, B. Humbert, Background removal from spectra by designing and minimising a non-quadratic cost function, Chemom. Intell. Lab. Syst., 76 (2005) 121–133.
[41] S. Sablani, M. Goosen, R. Al-Belushi, M. Wilf, Concentration polarization in ultrafiltration and reverse osmosis: a critical review, Desalination, 141 (2001) 269–289.
[42] A.L. Zydney, Stagnant film model for concentration polarization in membrane systems, J. Membr. Sci., 130 (1997) 275–281.
[43] R. Sheikholeslami, M. Ng, Calcium sulfate precipitation in the presence of nondominant calcium carbonate: thermodynamics and kinetics, Ind. Eng. Chem. Res., 40 (2001) 3570–3578.
[44] Ch. Tzotzi, T. Pahiadaki, S.G. Yiantsios, A.J. Karabelas, N. Andritsos, A study of $CaCO_3$ scale formation and inhibition in RO and NF membrane processes, J. Membr. Sci., 296 (2007) 171–184.
[45] C. Carteret, A. Dandeu, S. Moussaoui, H. Muhr, B. Humbert, E. Plasari, Polymorphism studied by lattice phonon Raman spectroscopy and statistical mixture analysis method. Application to calcium carbonate polymorphs during batch crystallization, Cryst. Growth Des., 9 (2009) 807–812.
[46] M. De La Pierre, C. Carteret, L. Maschio, E. André, R. Orlando, R. Dovesi, The Raman spectrum of $CaCO_3$ polymorphs calcite and aragonite: a combined experimental and computational study, J. Chem. Phys., 140 (2014) 164509.
[47] N. Buzgar, A. Ionu, Ț. Apopei, The Raman Study of Certain Carbonates, (n.d.) 16.
[48] L. Borromeo, U. Zimmermann, S. Andò, G. Coletti, D. Bersani, D. Basso, P. Gentile, B. Schulz, E. Garzanti, Raman spectroscopy as a tool for magnesium estimation in Mg-calcite, J. Raman Spectrosc., 48 (2017) 983–992.
[49] J. Schindelin, I. Arganda-Carreras, E. Frise, V. Kaynig, M. Longair, T. Pietzsch, S. Preibisch, C. Rueden, S. Saalfeld, B. Schmid, J.-Y. Tinevez, D.J. White, V. Hartenstein, K. Eliceiri, P. Tomancak, A. Cardona, Fiji: an open-source platform for biological-image analysis, Nat. Methods, 9 (2012) 676–682.
[50] E. Lyster, Y. Cohen, Numerical study of concentration polarization in a rectangular reverse osmosis membrane channel: permeate flux variation and hydrodynamic end effects, J. Membr. Sci., 303 (2007) 140–153.
[51] K.D. Cobry, Z. Yuan, J. Gilron, V.M. Bright, W.B. Krantz, A.R. Greenberg, Comprehensive experimental studies of early-stage membrane scaling during nanofiltration, Desalination, 283 (2011) 40–51.
[52] Y. Osada, T. Nakagawa, Membrane Science and Technology, CRC Press, Boca Raton, 2014.
[53] C. Zhu, N. Tong, L. Song, G. Zhang, Investigation of Raman Spectra of Polyethylene Terephthalate, in: Int. Symp. Photonics Optoelectron. 2015, SPIE, 2015, pp. 72–76.
[54] P. Matousek, I.P. Clark, E.R.C. Draper, M.D. Morris, A.E. Goodship, N. Everall, M. Towrie, W.F. Finney, A.W. Parker, Subsurface probing in diffusely scattering media using spatially offset Raman Spectroscopy, Appl. Spectrosc., 59 (2005) 393–400.
[55] M.J. Pelletier, Quantitative analysis using Raman Spectrometry, Appl. Spectrosc., 57 (2003) 20A–42A.
[56] B.P. Kafle, Chapter 8 – Raman Spectroscopy, B.P. Kafle, Ed., Chem. Anal. Mater. Charact. Spectrophotometry, Elsevier, 2020, pp. 245–268.
[57] C.Y. Tai, F.-B. Chen, Polymorphism of $CaCO_3$, precipitated in a constant-composition environment, AIChE J., 44 (1998) 1790–1798.
[58] M. Brusilovsky, J. Borden, D. Hasson, Flux decline due to gypsum precipitation on RO membranes, Desalination, 86 (1992) 187–222.
[59] N. Feoktistova, J. Rose, V.Z. Prokopović, A.S. Vikulina, A. Skirtach, D. Volodkin, Controlling the vaterite $CaCO_3$ crystal pores. Design of tailor-made polymer based microcapsules by hard templating, Langmuir, 32 (2016) 4229–4238.
[60] A. Niedermayr, S.J. Köhler, M. Dietzel, Impacts of aqueous carbonate accumulation rate, magnesium and polyaspartic acid on calcium carbonate formation (6°C–40°C), Chem. Geol., 340 (2013) 105–120.
[61] T. Waly, M.D. Kennedy, G.-J. Witkamp, G. Amy, J.C. Schippers, The role of inorganic ions in the calcium carbonate scaling of seawater reverse osmosis systems, Desalination, 284 (2012) 279–287.
[62] M. Sudmalis, R. Sheikholeslami, Coprecipitation of $CaCO_3$ and $CaSO_4$, Can. J. Chem. Eng., 78 (2000) 21–31.
[63] J. Liu, Z. Li, Y. Wang, X. Liu, G. Tu, W. Li, Analyzing scaling behavior of calcium sulfate in membrane distillation via optical coherence tomography, Water Res., 191 (2021) 116809.
[64] A.E.S. Van Driessche, T.M. Stawski, L.G. Benning, M. Kellermeier, Calcium Sulfate Precipitation Throughout Its Phase Diagram, A.E.S. Van Driessche, M. Kellermeier, L.G. Benning, D. Gebauer, Eds., New Perspect. Miner. Nucleation Growth Solut. Precursors Solid Mater, Springer International Publishing, Cham, 2017, pp. 227–256.
[65] W. Beckmann, Crystallization: Basic Concepts and Industrial Applications, John Wiley & Sons, Incorporated, Weinheim, Germany, 2013.
[66] T.M. Stawski, A.E.S. van Driessche, M. Ossorio, J. Diego Rodriguez-Blanco, R. Besselink, L.G. Benning, Formation of calcium sulfate through the aggregation of sub-3 nanometre primary species, Nat. Commun., 7 (2016) 11177.
[67] S. Mitrouli, A.J. Karabelas, A. Karanasiou, M. Kostoglou, Incipient calcium carbonate scaling of desalination membranes in narrow channels with spacers—experimental insights, J. Membr. Sci., 425–426 (2013) 48–57.
[68] P. Dydo, M. Turek, J. Ciba, K. Wandachowicz, J. Misztal, The nucleation kinetic aspects of gypsum nanofiltration membrane scaling, Desalination, 164 (2004) 41–52.
[69] H.N.S. Wiechers, P. Sturrock, G.v.R. Marais, Calcium carbonate crystallization kinetics, Water Res., 9 (1975) 835–845.
[70] M.R. Christoffersen, J. Christoffersen, M.P.C. Weijnen, G.M. Van Rosmalen, Crystal growth of calcium sulphate dihydrate at low supersaturation, J. Cryst. Growth, 58 (1982) 585–595.
[71] J.J. De Yoreo, P.G. Vekilov, Principles of crystal nucleation and growth, Rev. Mineral. Geochem., 54 (2003) 57–93.